



Interglacial responses of the southern Greenland ice sheet over the last 430,000 years determined using particle-size specific magnetic and isotopic tracers



Robert G. Hatfield^{a,*}, Alberto V. Reyes^{b,c}, Joseph S. Stoner^a, Anders E. Carlson^{a,c}, Brian L. Beard^c, Kelsey Winsor^{c,d}, Bethany Welke^c

^a College of Earth, Ocean, and Atmospheric Science, Oregon State University, Corvallis, OR 97331, USA

^b Department of Earth and Atmospheric Sciences, University of Alberta, Edmonton, Alberta T6G 2E3, Canada

^c Department of Geoscience, University of Wisconsin-Madison, 1215 West Dayton Street, Madison, WI 53706, USA

^d Department of Environmental, Earth & Atmospheric Sciences, University of Massachusetts-Lowell, Lowell, MA 01854, USA

ARTICLE INFO

Article history:

Received 16 May 2016

Received in revised form 2 September 2016

Accepted 6 September 2016

Available online 30 September 2016

Editor: M. Frank

Keywords:

South Greenland ice sheet
sediment tracing
radiogenic isotopes
magnetic properties
quaternary climate change
sea-level rise

ABSTRACT

The past behavior of the Greenland ice sheet can provide important insight into climatic thresholds that may initiate and drive major ice-sheet retreat. Particle-size-specific magnetic and Sr–Nd–Pb isotope records from Eirik Ridge sediments south of Greenland track southern Greenland ice sheet (sGIS) erosional signatures over the past ~430 ka by discriminating changes in sediment source and transport over the Eirik Ridge. Ground-truthed magnetic and isotopic compositions of subglacial silt from south Greenland's Precambrian bedrock terranes constrain independent magnetic and isotopic estimates of Eirik Ridge silt provenance, which in turn indicate that the southern Greenland ice sheet (sGIS) retreated within its present margin during three of the four previous interglaciations over the past ~430 ka. Retreat of the sGIS was extensive during the Marine Isotope Stage (MIS) 5e, 9, and 11 interglaciations, continuing unabated despite declining insolation during MIS 5e and 9, with near complete deglaciation in MIS 11. Retreat of the sGIS during MIS 7 was minimal, notwithstanding strong insolation forcing, while Holocene retreat slowed shortly after peak insolation. The reconstruction of sGIS retreat during the last five deglacial and interglacial periods suggests that a threshold for extensive sGIS retreat exists between the insolation and CO₂ states of the Holocene and the MIS 5e and 9 interglaciations, with CO₂ exerting a stronger control on sGIS retreat than insolation. Our results also suggest that the extent and stability of the sGIS in the Holocene is anomalous in the context of late-Quaternary interglaciations.

© 2016 Elsevier B.V. All rights reserved.

1. Introduction

Future changes in the volume of Earth's ice sheets will have important environmental, economic, and societal impacts. Past climate conditions, including times both warmer and cooler than present, provide a means of assessing ice-sheet thresholds and responses to changes in Earth's radiative budget (Tzedakis et al., 2009; Carlson and Winsor, 2012; Past Interglacials Working Group of PAGES, 2016). The terrestrial geological record provides the most direct evidence for paleo ice-sheet extent and behavior (e.g. Bennike and Björck, 2002; Carlson and Winsor, 2012; Funder et al., 2011), but such records are limited to the last deglaciation, as earlier evidence was largely erased during glacial advance. Marine

sediments, in contrast, can provide well-dated evidence of ice-sheet retreat and advance through glacial–interglacial cycles once sediment source signatures are linked to points of ice-sheet discharge (Carlson et al., 2008; Colville et al., 2011; Reyes et al., 2014; White et al., 2016).

Labrador Sea sediments can provide continuous records of ice-sheet and ocean interactions (e.g., Carlson et al., 2008; Evans et al., 2007; Fagel et al., 2002, 2004; Fagel and Hillaire-Marcel, 2006; Innocent et al., 2000; Hillaire-Marcel et al., 1994; Stanford et al., 2006; Stoner et al., 1995; Winsor et al., 2012). Magnetic, geochemical, and radiogenic-isotope records from Eirik Ridge south of Greenland document changes in the sourcing of sediment from Precambrian Greenland (PG) terranes during glacial terminations and interglaciations that can be used to track ablation of the southern Greenland ice sheet (sGIS) and the magnitude of sGIS retreat (Carlson et al., 2008; Colville et al., 2011; Reyes et al., 2014; Stoner et al., 1995). However, a poor understanding of what drives

* Corresponding author.

E-mail address: rhatfiel@ceos.oregonstate.edu (R.G. Hatfield).

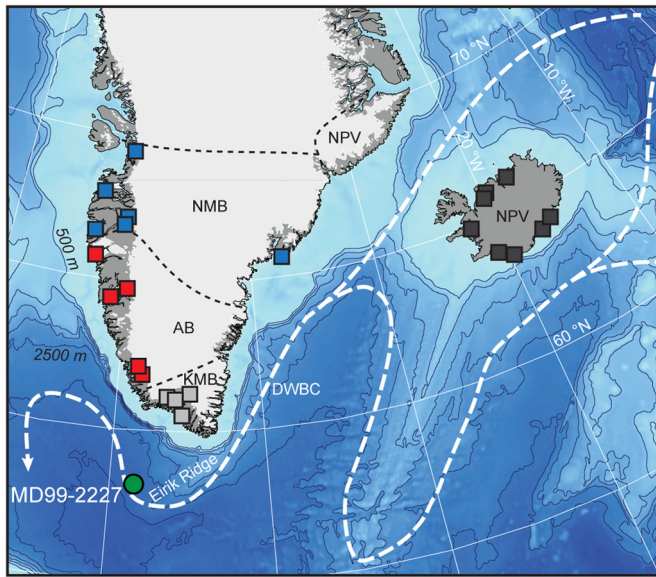


Fig. 1. Location of core MD99-2227 (green circle) and sampling sites of potential terrestrial sediment source terranes (Hatfield et al., 2013; Reyes et al., 2014); KMB, Ketilidian Mobile Belt (grey squares); AB, Archean Block (red squares); NMB, Nagssugtoqidian Mobile Belt (blue squares); NPV, Neogene and Paleogene Volcanics (black squares). Bedrock terrane boundaries are delineated (black dashed lines) and white dashed lines mark the modern-day Deep Western Boundary Current (DWBC) circulation path that is thought to have been active during interglaciations. (For interpretation of the references to color in this figure legend, the reader is referred to the web version of this article.)

bulk magnetic variation over the Eirik Ridge has meant increases in silt proportion and coarsening bulk magnetic grain size in these records have also been interpreted to reflect changes in the transport efficiency of PG and Neogene and Paleogene Volcanic (NPV) sediment from Iceland and East Greenland due to changes in the position and strength of the Deep Western Boundary Current (DWBC) (Evans et al., 2007; Hall et al., 1989; Mazaud et al., 2012; Stanford et al., 2006) (Fig. 1). PG silt sources from the three terranes of southern Greenland, the Ketilidian Mobile Belt (KMB), Archean Block (AB), and Nagssugtoqidian Mobile Belt (NMB), can be discriminated from the NPV (Fig. 1) using silt Sr–Nd–Pb isotope composition, which is controlled by differences in the age and tectonometamorphic history of these terranes (Colville et al., 2011; Reyes et al., 2014). Similarly, the ratio of saturation remanence (M_{rs}) to saturation magnetization (M_s), as a proxy for ferrimagnetic grain size (Day et al., 1977), has recently shown that PG silt-sized sediments are magnetically coarser (M_{rs}/M_s range 0.03–0.15) and distinct from the magnetically finer (M_{rs}/M_s range 0.20–0.32) NPV silts, while their corresponding clay fractions are less easily distinguished (Hatfield et al., 2013).

Because silt-size PG and NPV sediment sources have distinct magnetic (Hatfield et al., 2013) and Sr–Nd–Pb isotopic (Colville et al., 2011; Reyes et al., 2014) signatures, we can isolate the PG signature that can be related to sGIS ablation, sediment export, and retreat, from NPV signatures related to changes to the DWBC (e.g., Fagel et al., 2004; Fagel and Hillaire-Marcel, 2006). We combine new (MIS 10–9 and 8–7) and previously published (MIS 2–1, 6–5e and 12–11; Colville et al., 2011; Reyes et al., 2014) Eirik Ridge silt Sr–Nd–Pb isotope data with new sediment texture data and a new high-resolution magnetic proxy (silt M_{rs}/M_s) to trace the behavior of the sGIS through the last five glacial terminations and interglaciations. We then compare our independent datasets to changes in radiative forcing since MIS 12 (~430 ka) in order to provide a first record of sGIS response to climate forcing over the last five glacial–interglacial transitions.

2. Materials and methods

2.1. Site setting, age model, and sediment sampling

Our analysis is based on the 43 m sedimentary record from MD99-2227 (58.12°N, 48.22°W, 3460 m water depth) collected during the IMAGES-V Leg II from the Marion Dufresne II. MD99-2227 was cored on the lee side of the southwestern extremity of the Eirik Ridge (Fig. 1) where sediments accumulate rapidly during interglacials in response to a deepening of the DWBC (Hillaire-Marcel et al., 1994; Hunter et al., 2007). Eirik Ridge is a Plio-Pleistocene depositional structure conditioned by sediment redeposition as a result of DWBC flow off south Greenland (Hunter et al., 2007). Subglacial erosion beneath the Greenland, Iceland and Laurentide ice sheets, continental export, and subsequent redistribution by the DWBC delivers abundant terrigenous sediment to Eirik Ridge, with rapidly deposited detrital layers commonly observed during times of ice sheet instability (Hillaire-Marcel et al., 1994; Stoner et al., 1995; Evans et al., 2007; Hunter et al., 2007; Carlson et al., 2008). Lithology reflects these environmental variations and ranges from silty clay with sand and little biogenic material during glacial and deglacial times, to homogeneous nannofossil ooze with silty clay and common bioturbation during interglaciations (Hillaire-Marcel et al., 1994; Fagel and Hillaire-Marcel, 2006; Evans et al., 2007).

Our MD99-2227 age model is based on ^{14}C and $\delta^{18}\text{O}$ records from planktonic foraminifera and relative (geomagnetic) paleointensity (RPI). We supplement the existing single species (*Neoglobobulimina pachyderma* (sinistral)) MD99-2227 planktonic foraminifera $\delta^{18}\text{O}$ records (Evans et al., 2007; Reyes et al., 2014; Winsor et al., 2012) for MIS 8–7 and MIS 10–9 with 44 additional analyses of the same single species picked from the 150–250 μm fraction and measured at the Stable Isotope Laboratory at Oregon State University following Winsor et al. (2012). For the glacial–interglaciation intervals MIS 2–1, MIS 6–5, MIS 8–7, and MIS 12–11, we take advantage of published age models. The MIS 2–1 chronology is established using 23 ^{14}C dates for the last ~24 ka (Carlson et al., 2008) while for MIS 6–5, MIS 8–7, and MIS 12–11 it is based on the tandem correlation of RPI (Evans et al., 2007) and the $\delta^{18}\text{O}$ record of planktic foraminifera (Evans et al., 2007; Reyes et al., 2014; Winsor et al., 2012; this study) to the PISO-1500 RPI and $\delta^{18}\text{O}$ stacked records (Channell et al., 2009; Reyes et al., 2014). The chronology of PISO-1500 is established by first tuning individual RPI and $\delta^{18}\text{O}$ records to those of Integrated Ocean Drilling Program (IODP) Site U1308 (Channell et al., 2008, 2009; Hodell et al., 2008). The IODP Site U1308 benthic $\delta^{18}\text{O}$ record (Hodell et al., 2008) was then tuned to the benthic LR04 $\delta^{18}\text{O}$ stack (Lisiecki and Raymo, 2005) to generate the PISO-1500 age model (Channell et al., 2009).

Benthic foraminifera are scarce in IODP Site U1308 during the MIS 10–9 interval (Hodell et al., 2008), resulting in chronological uncertainties in the IODP Site U1308 and PISO-1500 age models relative to LR04 during this time interval. Planktic foraminifera are also scarce during Termination 4 (T4) in MD99-2227 (Fig. 2b) making it difficult to establish a chronology through direct tuning of the MD99-2227 $\delta^{18}\text{O}$ record to LR04 (Fig. 2a). To circumvent this issue, we retune the RPI record of MD99-2227 during MIS 10–9 (Fig. 2d; Evans et al., 2007) to the RPI record of Ocean Drilling Program (ODP) Site 983 (Channell, 1999) on its improved ODP Site 1089 tuned chronology (Stoner et al., 2003) (Fig. 2c). Fifteen tie points were used to generate the MD99-2227 MIS 10–9 age model (Figs. 2c, d). The full, integrated (new and published data), MD99-2227 $\delta^{18}\text{O}$ record is shown alongside LR04 in Fig. 3.

Using this chronology as a guide, we collected ~3 cm³ subsamples, typically at 10 cm intervals, between 2400–2990 cm (MIS 8–7) and 3430–3650 cm (MIS 10–9) for magnetic and radiogenic isotope analyses. Sand (>63 μm) was separated by wet sieving;

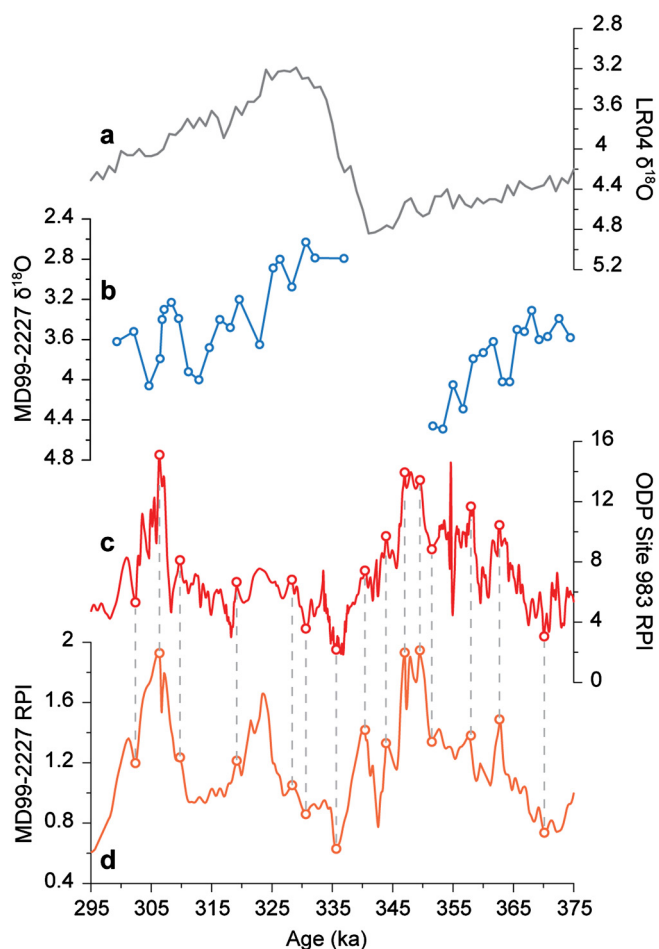


Fig. 2. MIS 10–9 age model for MD99-2227. (a) LR04 benthic $\delta^{18}\text{O}$ stack (Lisiecki and Raymo, 2005); (b) planktic $\delta^{18}\text{O}$ *N. pachyderma* (s) record (Evans et al., 2007) on the age model generated by correlation of the MD99-2227 RPI record (d) (Evans et al., 2007) to the ODP Site 983 RPI record (c) (Channell, 1999) on its improved ODP Site 1089 tuned chronology (Stoner et al., 2003). Correlation is achieved using fifteen tie points (open circles and gray lines) and circumvents the poorly defined $\delta^{18}\text{O}$ record in MD99-2227.

silt (3–63 μm) and clay (<3 μm) fractions were isolated by settling following Stokes law. Silt Sr–Nd–Pb data in MD99-2227 are published for MIS 2–1 and MIS 6–5e (Colville et al., 2011) and MIS 12–11 (Reyes et al., 2014). For the new magnetic analyses of these intervals, we subsampled at similar (~ 10 cm) spacing between 0–700 cm (MIS 2–1), 1750–2170 cm (MIS 6–5), and 3850–4280 cm (MIS 12–11) and where possible incorporated the same samples as those previously measured for radiogenic isotopes to facilitate direct comparison of the two records (85% of the new and published radiogenic data points have a corresponding magnetic measurement). Sediment fractions were weighed to generate the percent that fraction contributed to the bulk sediment by weight (wt.%) and to facilitate calculation of mass-normalized magnetic properties. Limiting our analyses of both sedimentary source (Colville et al., 2011; Reyes et al., 2014; Hatfield et al., 2013) and sink to the identical silt size fraction provides multiple benefits. It allows us to focus on the size fraction that is a dominant product of subglacial erosion (Cowton et al., 2012) and has the greatest magnetic source discrimination (Hatfield et al., 2013), while avoiding provenance complications associated with long distance transport of clays (e.g. Fagel et al., 2002; Fagel and Hillaire-Marcel, 2006) or coarse ice-rafted debris (e.g. White et al., 2016). Importantly, use of a single grain-size fraction for endmembers and provenance unknowns avoids the potential for grain size dependence of both

isotopic (e.g. Innocent et al., 2000) and magnetic (Hatfield et al., 2013) parameters.

2.2. Radiogenic isotope analyses

Sample preparation and isotope analyses (other than Pb) of the detrital silt fraction followed Reyes et al. (2014) and are only summarized here. Twenty eight acid-leached, spiked, and digested silt samples from MIS 8–7 and 10–9 intervals of MD99-2227 were separated by ion exchange column chromatography, and isotope ratios measured on a VG Sector 54 thermal ionization mass spectrometer (Sr, Rb, Nd) and a Micromass IsoProbe multiple-collector inductively-coupled-plasma mass spectrometer (Pb, Sm). Concentrations of Rb, Sr, Nd, and Sm were determined by isotope dilution. Procedural blanks were negligible compared to sample size, so no blank correction was applied. All isotope preparations and measurements were conducted at the University of Wisconsin Radiogenic Isotope Facility. Isotope results are presented in full in Supplementary Table 1; isotopic analyses of NIST and USGS secondary standards are provided in Supplementary Tables 2 (Pb) and 3 (Sr, Nd).

Pb isotope ratios were measured on a Micromass IsoProbe using NIST SRM-997 Tl for internal normalization of Pb isotope ratios to a constant $^{203}\text{Tl}/^{205}\text{Tl}$. Pb isotope ratios are reported relative to a bracketing standard of NIST SRM-981 Pb (Pb/Tl = 10), where the Pb isotope ratios of Galer and Abouchami (1998) are used. For comparison, we measured as samples NIST SRM-982, SRM-981, and SRM-1400, and USGS rock standards BCR-2 and AGV-2, over the same range of Pb/Tl (Pb/Tl weight ratio ranged from 10 to 6). The Pb isotope ratios of these standards agree well with values reported from the literature (Supplementary Table 3). Typical reproducibility of Pb isotope ratios is 0.024% per amu. Isotope analysis of Pb included a one-minute on-peak zero measurement followed by 40 10-s on-peak integrations with a typical ^{208}Pb ion signal of 4×10^{-11} amps. Isobaric interference of ^{204}Hg was monitored at ^{202}Hg and ^{201}Hg , and was insignificant following on-peak zero subtraction.

The Sr, Nd, and Pb isotope composition of the silt size fraction in MD99-2227 can discriminate NPV from PG sediment sources and, when constrained by extensive ground-truthing of similar size fractions (Colville et al., 2011; Reyes et al., 2014), can discriminate sediment sources from south Greenland's three Precambrian bedrock terranes (NMB, AB, and KMB; Fig. 4). KMB silts are distinguishable from AB and NMB sediments by their higher $^{206}\text{Pb}/^{204}\text{Pb}$, $^{207}\text{Pb}/^{204}\text{Pb}$, and ϵ_{Nd} values (Fig. 4c–f). AB silts have the lowest ϵ_{Nd} and high $^{87}\text{Sr}/^{86}\text{Sr}$ values and are discriminable from NMB silts on the basis of their lower $^{207}\text{Pb}/^{204}\text{Pb}$ (Fig. 4c) and $^{208}\text{Pb}/^{204}\text{Pb}$ ratios. NPV silts from East Greenland and Iceland are characterized by their very low $^{87}\text{Sr}/^{86}\text{Sr}$ and high ϵ_{Nd} values (Fig. 4a, b, f), relative to PG sediments. To estimate sediment source proportions, we use the four terrane-component mixing model with five isotope-ratio end-members developed in Colville et al. (2011) and refined in Reyes et al. (2014). Briefly, the mixing model estimates the relative proportion of terrigenous silt in MD99-2227 that originated from subglacial bedrock erosion in the KMB, AB, NMB and NPV source regions. KMB, AB and NMB endmembers are based on concentration and isotope composition data of stream sediment silts from these terranes, to avoid misleading endmember compositions due to whole-rock or grain-size fractionation (Reyes et al., 2014), while the strongly contrasting NPV endmembers are based on compiled whole-rock data (Colville et al., 2011; Reyes et al., 2014).

Rather than relying on the arithmetic mean for endmembers, our model explicitly accounts for endmember uncertainty (Reyes et al., 2014). For each of ten evenly-spaced bins between the

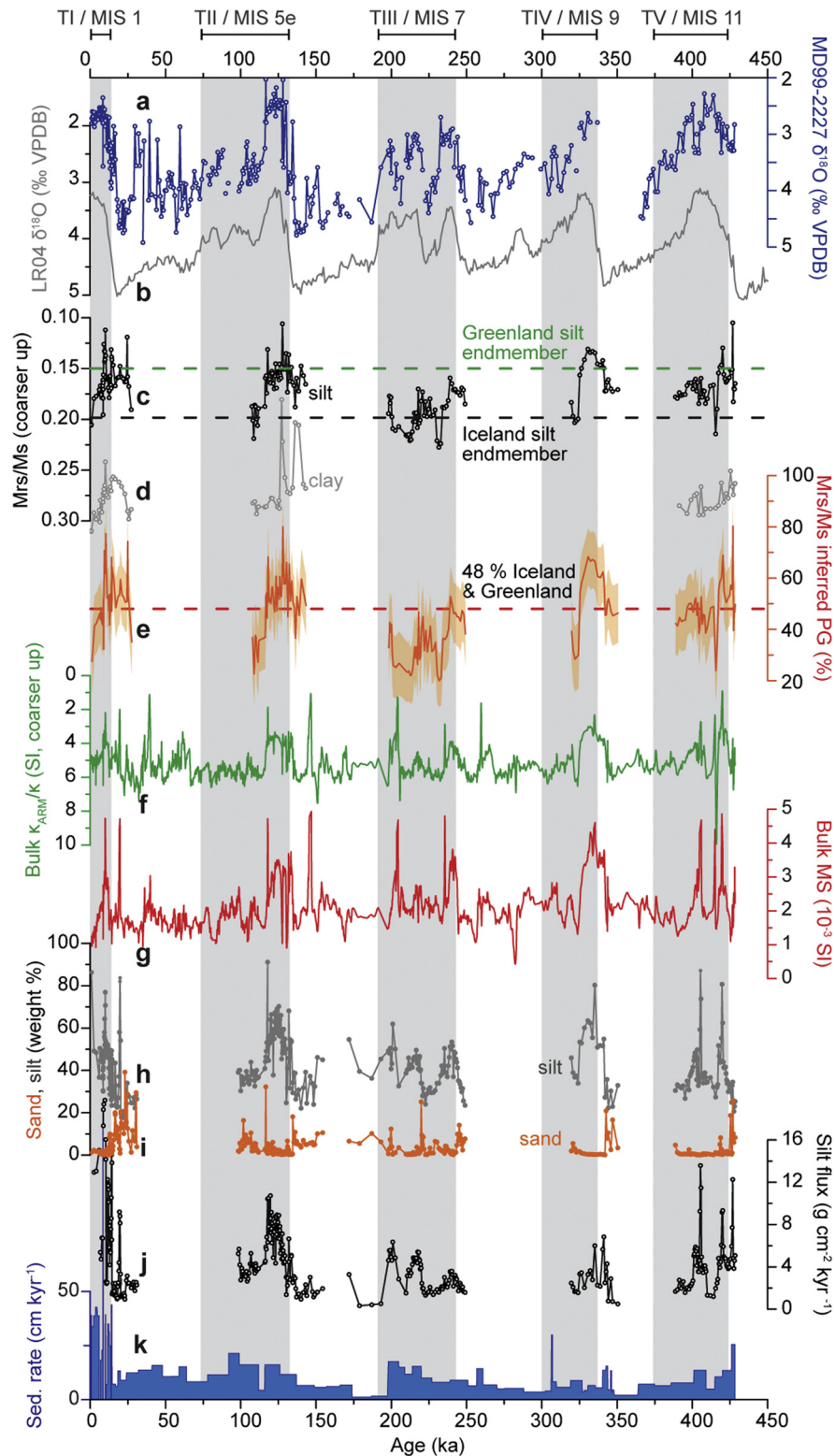


Fig. 3. Sediment properties of MD99-2227. (a) $\delta^{18}\text{O}$ *N. pachyderma* (s) record (Evans et al., 2007; Colville et al., 2011; Winsor et al., 2012; Reyes et al., 2014) compared to (b) LR04 benthic $\delta^{18}\text{O}$ stack (Lisiecki and Raymo, 2005). Silt (black; (c)) and clay (grey; (d)) Mrs/Ms values plotted against values that mark the limits of Greenland (<0.15) and Iceland (>0.20) terrestrial sources (Hatfield et al., 2013). (e) Average modeled PG% silt contribution (orange) based on Mrs/Ms unmixing, with 1 standard deviation (shading) and the MD99-2227 average of 48% (dashed line). (f) Bulk $\kappa_{\text{ARM}}/\kappa$ (green; as a proxy for bulk magnetic grain size) and (g) bulk magnetic susceptibility (red) records (Evans et al., 2007). (h) silt wt.% (grey), (i) sand wt.% (orange). (j) Silt flux (black), and (k) sedimentation rate (blue bars). Vertical grey bars denote the interglacial periods defined by LR04 (Lisiecki and Raymo, 2005). (For interpretation of the references to color in this figure legend, the reader is referred to the web version of this article.)

0.165 and 0.835 quantiles for each terrane geochemical dataset, we generated 1000 random end-member isotope composition and concentration combinations, for a total of 10,000 random combi-

nations of end-member values spanning 67% of the asymmetric probability envelope. We estimated Pb concentration for the four terranes using the arithmetic mean of Pb concentration estimated

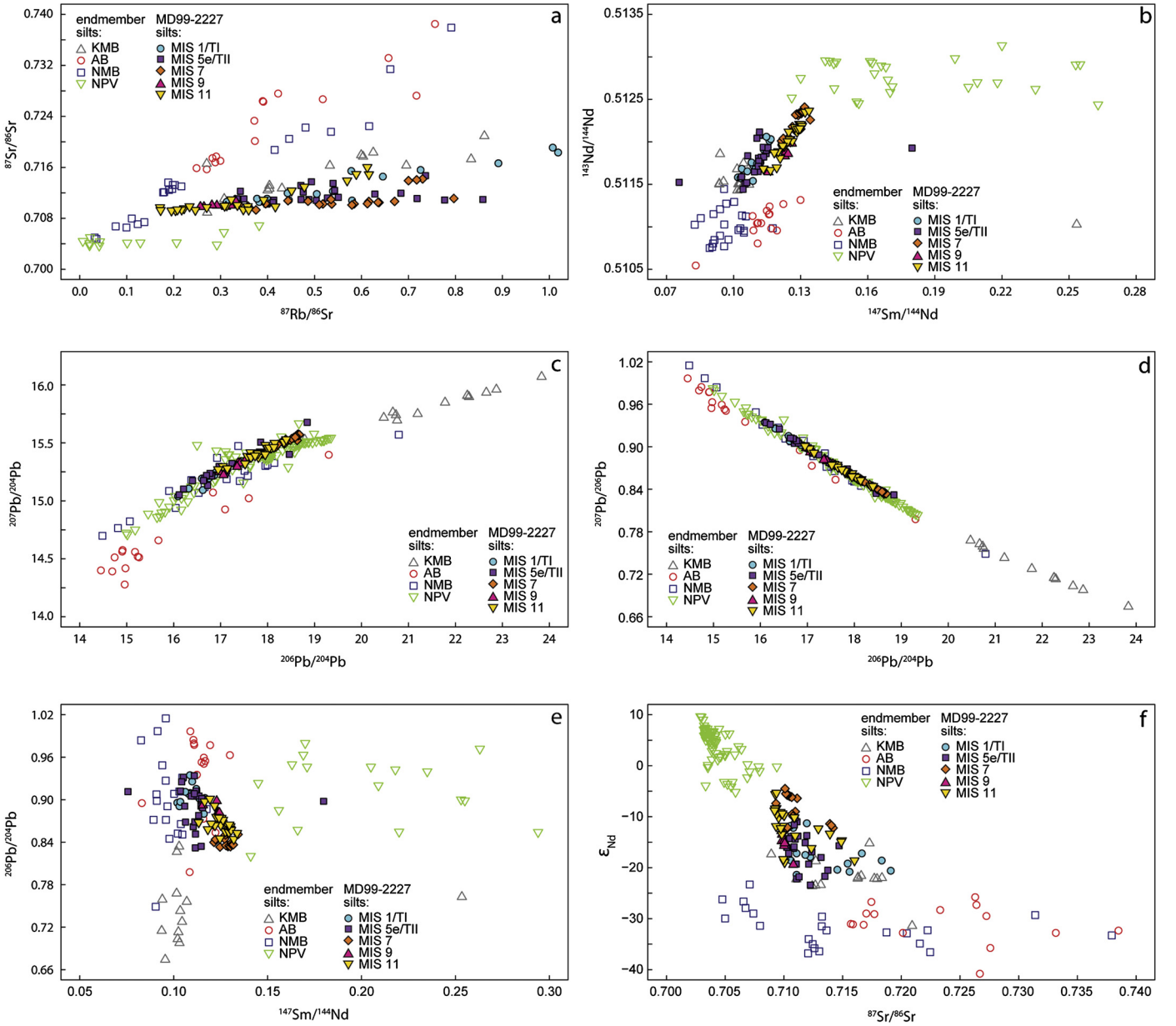


Fig. 4. Biplots of silt isotope composition for samples used to define terrane-component endmembers (open symbols) and MD99-2227 samples (closed symbols). Terrane endmember samples are glaciofluvial sediment and glaciogenic fines for KMB, AB, and NMB; NPV datapoints are wholerock and submerged shelf sediments compiled from the literature (Colville et al., 2011; Reyes et al., 2014). Mean/median mixing model endmember values and binary mixing lines are not indicated because the Monte Carlo simulation randomly samples from the frequency distribution of observed terrane-component endmembers for each of the 10,000 model-run iterations. MD99-2227 data for MIS 1/TI and MIS 5e/TII are from Colville et al. (2011); data for MIS 11 are from Reyes et al. (2014).

from mean continental crustal Pb/Sr and Pb/Nd ratios for each of the 10,000 randomly generated end-member combinations.

The four-component mixing model was implemented as:

$$R_m = \left\{ \left[f_{KMB}(C_e)_{KMB}(R_e)_{KMB} \right] + \left[f_{AB}(C_e)_{AB}(R_e)_{AB} \right] + \left[f_{NMB}(C_e)_{NMB}(R_e)_{NMB} \right] + \left[f_{NPV}(C_e)_{NPV}(R_e)_{NPV} \right] \right\} \times \left\{ \left[f_{KMB}(C_e)_{KMB} \right] + \left[f_{AB}(C_e)_{AB} \right] + \left[f_{NMB}(C_e)_{NMB} \right] + \left[f_{NPV}(C_e)_{NPV} \right] \right\}^{-1}$$

where:

R_m = the modeled isotope ratio

(ϵ_{Nd} , $^{87}Sr/^{86}Sr$, $^{206}Pb/^{204}Pb$, $^{207}Pb/^{204}Pb$, and $^{208}Pb/^{204}Pb$),

f = the terrane fraction of MD99-2227 $CaCO_3$ -free silt, and

$$f_{KMB} + f_{AB} + f_{NMB} + f_{NPV} = 1,$$

C_e = the end-member concentration for a given element (Sr, Nd, Pb),

R_e = end-member isotope ratio

(ϵ_{Nd} , $^{87}Sr/^{86}Sr$, $^{206}Pb/^{204}Pb$, $^{207}Pb/^{204}Pb$, and $^{208}Pb/^{204}Pb$).

The mixing equation was solved 10,000 times for each sample by iteratively increasing f by 0.01 and noting all values of f that gave R_m within a specified range (1.0 for ϵ_{Nd} , 0.0002 for $^{87}Sr/^{86}Sr$, 0.2 for $^{206}Pb/^{204}Pb$, 0.1 for $^{207}Pb/^{204}Pb$, and 0.2 for $^{208}Pb/^{204}Pb$) around the measured isotope ratios for that depth interval. Uncertainty estimates for the mixing model are provided by the 0.165–0.835

and 0.025–0.975 quantile range of valid mixing model solutions for each terrane, i.e. 67% and 95% confidence intervals (Supplementary Table 4). The Monte Carlo procedure for random end-member determination can yield unrealistic combinations of source terrane isotope composition and elemental concentration, so the uncertainties are conservative. Median mixing model results are corrected for CaCO_3 content, and are expressed as percent of total MD99-2227 sediment for each sample interval.

2.3. Magnetic analyses

Magnetic susceptibility (MS) of 309 clay and silt fractions was measured on a Bartington MS2B at 0.47 kHz in a field of $\sim 80 \text{ Am}^{-1}$ at the Oregon State University Paleomagnetic and Environmental Magnetic Laboratory. MS measurements were corrected for the diamagnetic properties of the sample containers before calculation of mass specific MS. Ms and Mrs of 286 clay and silt fractions was acquired by measurement of the major hysteresis loop with a saturating field of 1000 mT using a Princeton Measurements Corporation vibrating sample magnetometer at the Pacific Northwest Paleomagnetism Laboratory at Western Washington University. After high field slope correction at 800 mT, these parameters were combined (Mrs/Ms) and used as a proxy for ferrimagnetic grain size where lower (higher) Mrs/Ms values correspond to coarser (finer) magnetic grain sizes (Day et al., 1977). Mean PG% contribution values and their standard deviation are generated from two end-member linear unmixing of each MD99-2227 measured silt Mrs/Ms value against 10,000 iterations of Greenland and Iceland source end-member combinations picked from a normal distribution of measured Iceland (Mrs/Ms range = 0.20–0.32) and Greenland (Mrs/Ms range = 0.03–0.15) terrestrial silt samples (Hatfield et al., 2013). A 50:50 mix of PG and NPV sources yields a modeled Mrs/Ms value of 0.166 which falls close to the observed midpoint (0.173) between the two terrestrial end-member limits (0.20 for Iceland, 0.15 for Greenland) defined by Hatfield et al. (2013), suggesting that linear unmixing accurately reflects the source end-members and is sensitive to changing source fluxes. The full suite of magnetic data can be found in Supplementary Table 5.

3. Results

3.1. Sediment properties of MD99-2227

Down core analyses show increased proportions of silt (Fig. 3h), higher bulk magnetic concentrations (Fig. 3g), and coarser magnetic grain-size during interglaciations (Fig. 3f) in MD99-2227 that contrasts with the general North Atlantic pattern where glacial periods tend to have higher bulk magnetic concentration and coarser bulk magnetic grain size associated with ice rafting (e.g. Channell et al., 2008; Robinson, 1986). Because the median MS of the MD99-2227 silt fraction is ~ 6 times higher than that of the clay fraction (Fig. 5), high bulk MS during interglaciations (Fig. 3g) largely reflects the high silt wt.% (Fig. 3h). Additionally, interglacial intervals tend to have higher sedimentation rates (Fig. 3k) with these general patterns consistent with other records from across deeper parts of the Eirik Ridge (Evans et al., 2007; Hillaire-Marcel et al., 1994; Stoner et al., 1995). While we consider the sGIS and the DWBC as the principal mechanisms dictating the delivery of silt to MD99-2227 as observed during MIS 1 and 5e (Colville et al., 2011), some of the PG silt could also be transported in icebergs and/or sea ice. These processes are identified by high sand ($>63 \mu\text{m}$) wt.% in MD99-2227 (Fig. 3i) and are more prevalent during full glacial conditions (average $>10\%$, max. = 39%), reflecting extensive marine-terminating sGIS margins. Average sand

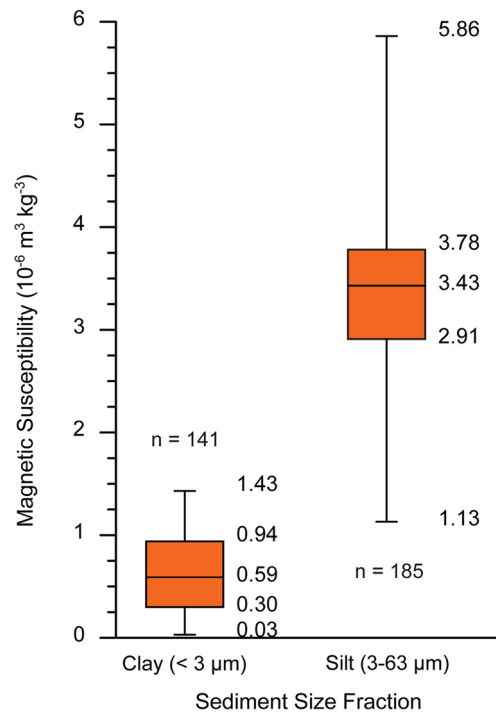


Fig. 5. Box whisker plots of magnetic susceptibility for the clay and silt fractions from MD99-2227. Median values (central black line) are six times greater in the silt fraction than the clay fraction. Box limits mark the upper (75%) and lower (25%) quartiles and whiskers the full range of the dataset.

wt.% falls to $<2\%$ (Fig. 3i) through the terminations and interglaciations, indicating that ice rafting is not significant during these periods.

Silt Mrs/Ms values in MD99-2227 are magnetically coarser (average = 0.17; range = 0.105–0.227) (Fig. 3c) than clay Mrs/Ms values (average = 0.273; range = 0.181–0.31) (Fig. 3d) demonstrating an inter-fraction variability that is characteristic of PG sources (Hatfield et al., 2013). Average modeled PG% values are indistinguishable from median modeled PG% values and suggest PG% contributions range from 81–20% (Fig. 3e), averaging 48% in MD99-2227. Low silt Mrs/Ms (Fig. 3c) and high PG contributions (Fig. 3e) are consistently accompanied by high silt wt.% (Fig. 3h), silt flux (Fig. 3j), and increased sedimentation rate (Fig. 3k), suggesting glacial terminations and interglaciations are characterized by an increased flux of PG sourced material.

In addition to the new high-resolution grain-size-specific magnetic data for the last five glacial terminations and interglaciations, new lower-resolution Sr–Nd–Pb isotope data for MIS 10 through MIS 7 are shown in Fig. 6. These data complement existing Sr–Nd–Pb isotope records for the last two deglacial/interglacial periods (MIS 6–1; Colville et al., 2011) and for MIS 12–11 (Reyes et al., 2014). Sample density for Sr–Nd–Pb isotope (and Mrs/Ms) analyses is limited for the MIS 9 and 7 interglaciations (Fig. 6), because we avoided high sand wt.% core intervals, which complicate isotopic discrimination of unique PG sediment sources due to potential for abundant ice-rafted detrital sediment input.

Seven silt samples through latest MIS 10 into MIS 9 have $^{87}\text{Sr}/^{86}\text{Sr}$ from ~ 0.711 to ~ 0.710 , and overall trends of increasing ϵ_{Nd} (-19 to -13) and more radiogenic Pb isotope ratios (Fig. 6d). For MIS 7e and 7c, $^{87}\text{Sr}/^{86}\text{Sr}$ is relatively consistent between ~ 0.711 and ~ 0.710 with an abrupt shift to more radiogenic values during MIS 7a (Fig. 6c). Silt ϵ_{Nd} is more variable, with lower values during MIS 7e (~ -13 to -10) than MIS 7c (~ -6), and an abrupt MIS 7a shift from -6 to -12 that mimics the abrupt shift to higher $^{87}\text{Sr}/^{86}\text{Sr}$ (Fig. 6c). Pb isotope ratios trend towards

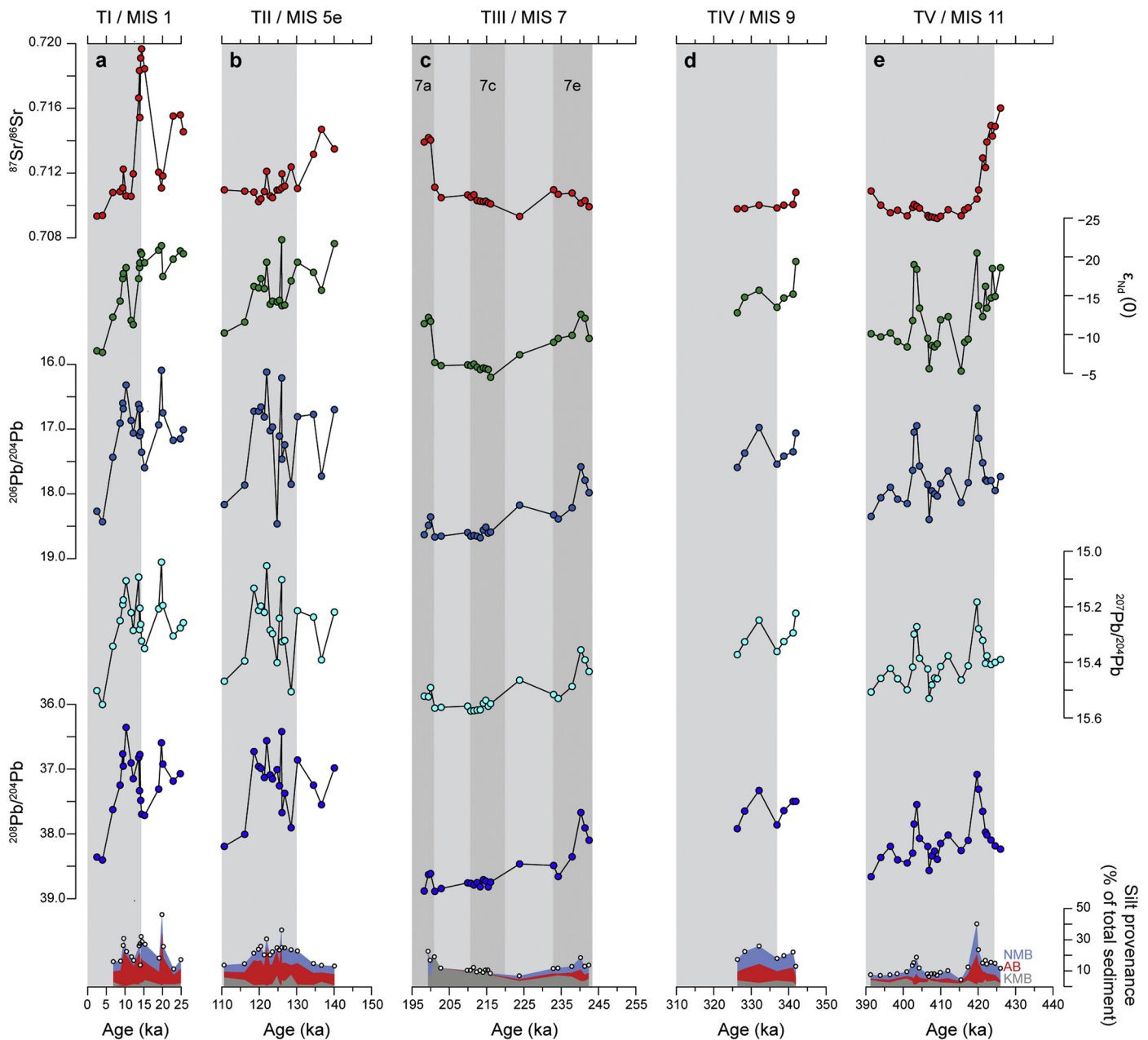


Fig. 6. Isotopic composition of MD99-2227 silt for (a) MIS 2–1, (b) MIS 6–5, (c) MIS 8–7, (d) MIS 10–9, and (e) MIS 12–11. Analytical uncertainty is smaller than symbol size. Axes are reversed for Nd and Pb data. The lowest panel shows the results of the five-component, four endmember mixing model. Median contributions from the KMB (gray), AB (red), and NMB (blue) are expressed as percent of the total sediment. Vertical light gray bars denote the interglacial periods defined by LR04 (Lisiecki and Raymo, 2005) and are the same as those in Fig. 3, darker gray bars in MIS 7 refer to the warmer sub-stages as defined by lower $\delta^{18}\text{O}$ values in MD99-2227. MIS 10–9 and MIS 8–7 isotope and mixing data are new results from this manuscript, MIS 2–1 and MIS 6–5 isotope and mixing data are from Colville et al. (2011), and MIS 12–11 isotope and mixing data are from Reyes et al. (2014). (For interpretation of the references to color in this figure legend, the reader is referred to the web version of this article.)

more radiogenic values through MIS 7c, and are relatively constant through MIS 7c and 7a (Fig. 6c).

The Sr–Nd–Pb isotope results indicate sustained PG-sourced silt in the MIS 9 interval of MD99-2227 and substantially lower PG-sourced silt contributions during MIS 7 (Fig. 4b, e, f). Results from the four-component isotope mixing model (Reyes et al., 2014) quantitatively support these qualitative inferences, and show reduced AB and NMB contributions through the MIS 7c and 7a substages (Fig. 6c). MIS 9 sediments are ~20–25% PG silt, with contribution from all three southern Greenland Precambrian terranes. The proportion of PG silt declines during MIS 7, with all three southern Greenland terranes contributing ~10–20% of PG

silt during MIS 7e. PG silt during MIS 7c comprises <13% of total sediment and is nearly completely derived from the KMB on southernmost Greenland. Sample density is particularly low for MIS 7a, but the four samples that yielded mixing model solutions indicate ~12–20% PG silt, with initial contribution largely from the KMB.

3.2. Tracking sGIS behavior since MIS 12

Biplots of silt wt.% and magnetically estimated PG% are divided into four quadrants using the average PG contribution of 48% (corresponding to a silt Mrs/Ms value of ~0.17) and the average silt content of 45 wt.% (Fig. 3h) to characterize high and low silt proportions (Fig. 7f). High proportions of silt derived from PG plot in

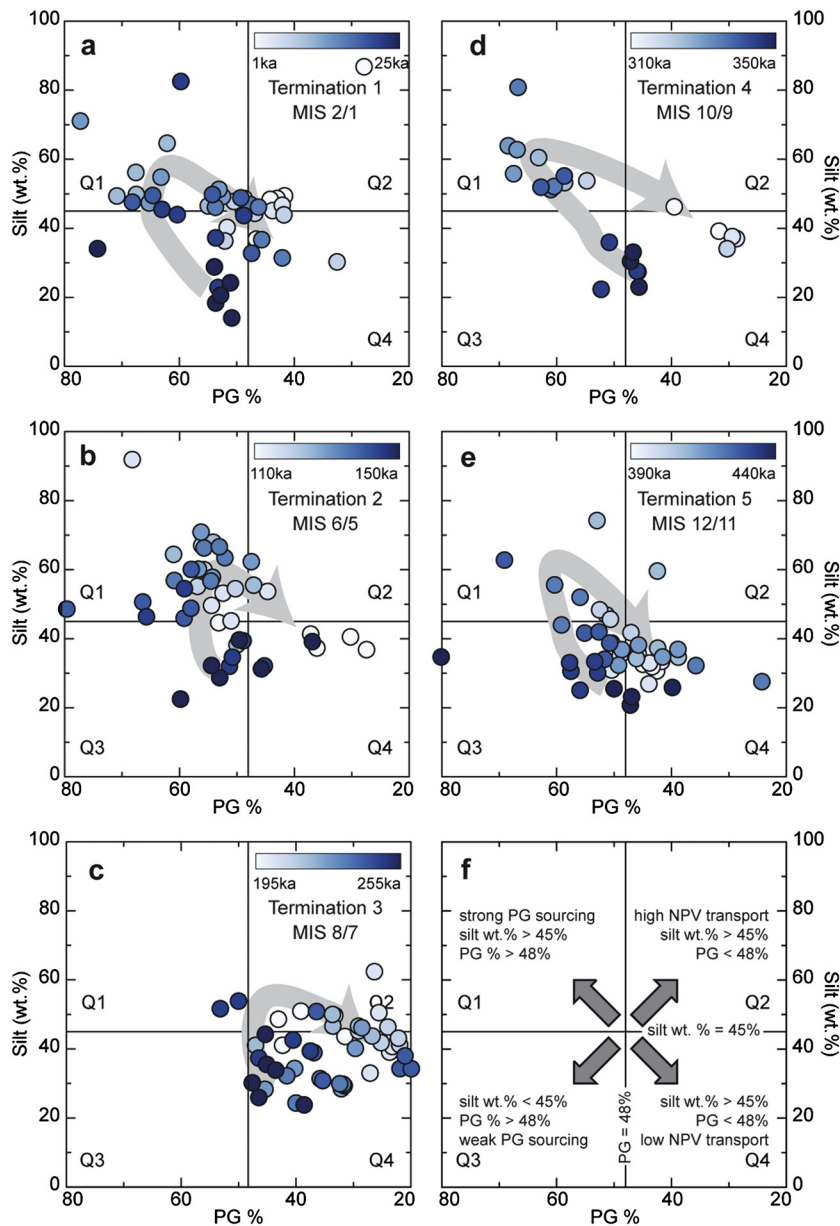


Fig. 7. Silt PG% vs silt wt.% quadrant plots for the last five glacial terminations and interglaciations (a–e). Colored symbols for PG % and silt wt.% data progress from dark (older) to light (younger) within each glacial termination and interglaciation. (f) Summary of quadrant plots interpretation. Quadrant plots are delineated using the average MD99-2227 silt PG % contribution (48%) and the average silt wt.% (45%). Arrows in (a–e) highlight the general deglacial progression from Q3 to Q1 sedimentation, followed by Q2 and/or Q4 sedimentation. (For interpretation of the references to color in this figure legend, the reader is referred to the web version of this article.)

Quadrant 1 (Q1), while high proportions of NPV silt transported by the DWBC fall into Q2. Relative to Q1, few samples fall into Q2 suggesting that glacial termination and interglacial increases in silt wt.% are predominantly sourced from PG (Fig. 7). Low PG% values coupled with low silt wt.% in Q4 likely reflects reduced transport of PG silt to the core site and continued deposition of NPV silt. Low PG% and silt wt.% define Q3, characterized by reduced transport of mainly PG silt to the site. Plotted individually, the last five glacial terminations and interglaciations follow a similar temporal evolution from Q3, through Q1, before shifting to Q4 and/or Q2 (Figs. 7a–e). We interpret this pattern as the sGIS deglacial silt signature. While this trend is broadly followed for each of the last five glacial terminations and interglaciations, differences in the duration of Q1 signatures suggest variations in the paleo-response of the sGIS to deglacial/interglacial climate forcing over the last ~430 ka (Fig. 8).

3.3. Glacial–interglacial changes

We validate our interpretive framework by comparing last deglacial and Holocene silt PG% signatures to well-dated glacial geological evidence, published and new radiogenic-isotope information, and marine proxy data. During the last glacial maximum and the early part of T1 (25–16 ka), relatively high ice-rafted debris (IRD) (high sand wt.% concentration (Fig. 3i) and Q3 signatures are consistent with calving from a marine-terminating sGIS on the continental shelf that is not discharging large amounts of PG silt (Funder et al., 2011; Lecavlier et al., 2014) (Fig. 7a). Increased ablation associated with a warming climate through the termination increases runoff and the delivery of water to the bed of the sGIS (Cowton et al., 2012; Hanna et al., 2008), and in turn promotes basal sliding, subglacial erosion (Cowton et al., 2012; Zwally et al., 2002) and meltwater export of glacial–fluvial silt-

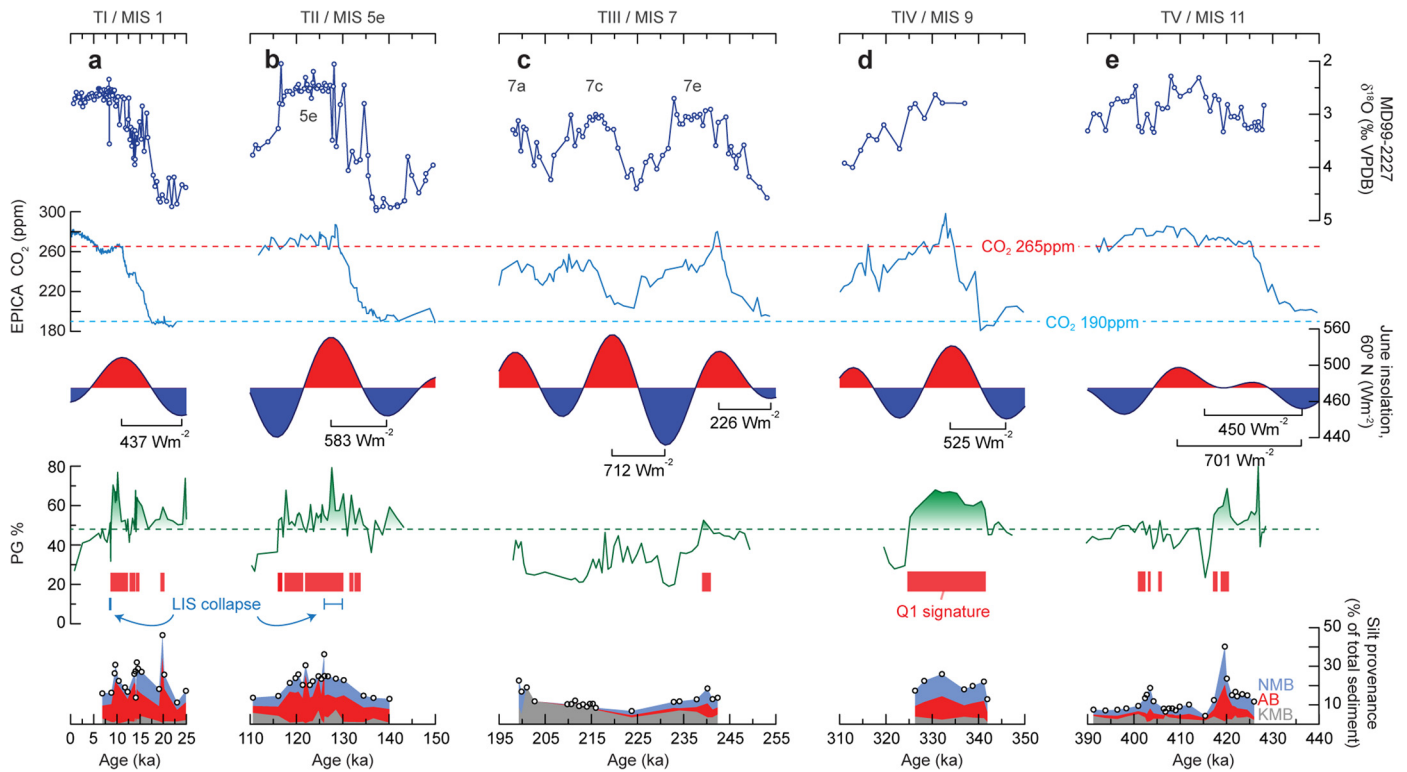


Fig. 8. Comparison of sediment data and potential forcings for (a) MIS 2/1, (b) MIS 6/5, (c) MIS 8/7, (d) MIS 10/9, and (e) MIS 12/11. From top to bottom in each panel: MD99-2227 $\delta^{18}\text{O}$ record; EPICA Dome C CO_2 concentration (ppm) annotated with typical glacial maxima concentrations of 190 ppm (blue dashed line) and early Holocene peak concentrations of 265 ppm (red dashed line) for reference (Lüthi et al., 2008); June 21st insolation at 60°N in Wm^{-2} , red (blue) shading denotes periods above (below) average insolation, cumulative accumulated insolation values are calculated as the increase above the insolation low over the range shown; modeled PG % silt contributions from Mrs/Ms unmixing, duration of Q1 signatures (red bars), and annotation of the timing of the collapse of the Laurentide ice sheet (LIS) (~ 8.4 ka for MIS 1/Holocene (Carlson, 2008) and between 127–129 ka for MIS 5e (Carlson, 2008; Colville et al., 2011; Nicholl et al., 2012)); and median inferred silt provenance estimated from the isotope mixing model expressed as percent of total sediment derived from KMB (grey), AB (red) and NMB (blue) terranes (Colville et al., 2011; Reyes et al., 2014). (For interpretation of the references to color in this figure legend, the reader is referred to the web version of this article.)

size sediment from southern Greenland to the ocean (Carlson et al., 2008; Cowton et al., 2012; Hanna et al., 2008; Reyes et al., 2014). In MD99-2227, this is manifested as an increase in sedimentation rate (Fig. 3k) and a shift to Q1 signatures (Fig. 7a). Quasi-continuous Q1 signatures begin ~ 15 ka and last until ~ 8 ka (Figs. 7a, 8a). The latter half of this period (~ 11 – 8 ka) is characterized by rapid and sustained increases in PG% and silt wt.% indicating increased intensity in the ablation and retreat of the sGIS (Figs. 7a, 8a). Similarly, Sr–Nd–Pb data also indicate increased ablation and PG silt supply (up to $\sim 30\%$ of total sediment) during these periods, but mixing model provenance estimates imply retention of the sGIS on all three of the southern Greenland PG terranes (Fig. 6a) (Colville et al., 2011). Q1 signatures cease and isotope-inferred Greenland contributions decrease at ~ 8 ka around the same time as terrestrial data suggest the sGIS stabilized (Carlson et al., 2014; Funder et al., 2011; Larsen et al., 2015) and shortly before the Laurentide ice sheet collapsed (Barber et al., 1999; Carlson, 2008) (Fig. 8a). Q2 signatures from 8–3 ka suggest a sGIS in quasi-equilibrium with Holocene climate near its present position, consistent with other terrestrial and marine observations (Carlson et al., 2008, 2014; Larsen et al., 2015; Lecavlier et al., 2014). Increased silt wt.% and Mrs/Ms values plotting in Q2 after ~ 3 ka agree with evidence for an intensified DWBC (Fagel et al., 2004).

MIS 6 has similar Q3 signatures and IRD proportions to the last glacial maximum (Figs. 3i, 7b). IRD decreases and Q1 signatures increase during T2. Q1 signatures are maintained through the $\delta^{18}\text{O}$ -minimum plateau of MIS 5e until ~ 116 ka when they shift to Q4 (Figs. 7b, 8b). A red sedimentary layer and Ca/Sr spike in Eirik Ridge cores at ~ 126 – 128 ka are attributed to the col-

lapse of the Laurentide ice sheet early in MIS 5e (Carlson, 2008; Colville et al., 2011; Nicholl et al., 2012). In comparison to the Holocene, when sGIS runoff decreased around the time of Laurentide ice-sheet deglaciation, our silt Mrs/Ms data indicate that elevated sGIS runoff and retreat continued for ~ 10 ka after Laurentide ice-sheet deglaciation during MIS 5e (Fig. 8b). The Sr–Nd–Pb isotope data are consistent with sustained sGIS retreat, with an ~ 10 ka interval characterized by high PG silt supply (~ 20 – 30% of total MD99-2227 silt) (Fig. 6b). The longer duration sGIS retreat suggests a smaller MIS 5e sGIS extent compared to the Holocene (Carlson et al., 2008; Colville et al., 2011; Stoner et al., 1995), though the isotope mixing model indicates that the sGIS remained on all three of the southern PG terranes (Colville et al., 2011) (Fig. 6b).

Following Q3 signatures in MIS 8, T3 and MIS 7 are dominated by Q4 signatures, have the shortest Q1 duration (confined to a brief portion of MIS 7e), and uniquely lack PG contributions $>55\%$ (Fig. 7c). Sand wt.% is higher throughout MIS 7 than during other interglaciations (Fig. 3i), likely reflecting extensive proximal marine-terminating ice margins in MIS 7 relative to other interglaciations. Our new silt Sr–Nd–Pb isotope data similarly indicate a brief pulse of silt sedimentation from PG sources during MIS 7e (Fig. 6c). However, the remainder of MIS 7 is characterized by low PG silt contributions ($<13\%$ of total sediment) that are nearly all sourced from the southernmost and most proximal PG terrane, the KMB. This provenance signal is likely due to the more radiogenic Pb isotope composition of MIS 7c and 7a silts, given that silt from KMB fluvial sediment has more radiogenic Pb isotope composition than the AB and NMB terranes, particularly for $^{206}\text{Pb}/^{204}\text{Pb}$ and $^{207}\text{Pb}/^{204}\text{Pb}$. The strong KMB provenance signal may be explained

by substantial ablation and associated subglacial erosion of KMB bedrock during MIS 7c and 7a, together with limited ablation and thus minimal delivery of subglacially eroded silt from the AB and NMB to the north (Fig. 1). Compared to the other interglaciations of the last ~430 ka, continued IRD (Fig. 3i) and the lack of strong runoff signatures in the silt magnetic (Fig. 7c) and isotopic proxies (Fig. 6c) suggest that sGIS did not retreat from the shelf during MIS 7. This is consistent with other North Atlantic marine sediment records and models that imply only modest warming during MIS 7 relative to other late Pleistocene interglaciations (Helmke and Bauch, 2003; Past Interglacials Working Group of PAGES, 2016; Tzedakis et al., 2009). Fagel and Hillaire-Marcel (2006) also suggested, based on Sm–Nd isotope analyses of the clay size fraction at ODP Site 646, that limited subglacial erosion of Precambrian North American Shield crust, which includes our PG endmembers, occurred in the North Atlantic basin during MIS 7.

T4 and MIS 9 are very similar in form to T2 and MIS 5e. Persistent Q1 signatures during T4 continue through the interglacial $\delta^{18}\text{O}$ -minimum plateau, before shifting to Q4 signatures at the end of the interglaciation (Figs. 7d, 8d). Q1 signatures with PG contributions >60% persist the longest of any of the last five interglaciations, implying sustained sGIS runoff and retreat during MIS 9 (Fig. 7d). Similar to MIS 5e, our lower temporal-resolution silt Sr–Nd–Pb data also indicate substantial terrigenous silt contributions (20–25% of total sediment) from all three PG terranes (Fig. 6d), consistent with retention of at least some ice on each south Greenland PG terrane.

Although sediments from MIS 12 were not completely recovered in MD99-2227, decreasing IRD and the shift from Q3 to Q1 indicates that T5 is well represented (Figs. 3i, 7e). Q1 signatures culminate with an abrupt excursion to Q4 during peak interglacial conditions, mimicking the silt Sr–Nd–Pb isotope data (Reyes et al., 2014) (Figs. 6e, 7e). The shift to very low PG input during MIS 11 is interpreted as indicating near complete deglaciation of southern Greenland (Reyes et al., 2014), alongside pollen (de Vernal and Hillaire-Marcel, 2008) and other proxy evidence for the warmest interglacial Arctic climate of the last half million years (Cronin et al., 2013; Melles et al., 2012). We note that while Q4 signatures also dominate MIS 7, the MIS 7 Q4 period does not follow an interval of elevated sGIS runoff and retreat inferred from sustained Q1 signatures and high silt contributions from all three south Greenland PG terranes (Reyes et al., 2014), as is the case with MIS 11. Thus the deglacial evolution of the silt magnetic and Sr–Nd–Pb records is what prompts our different interpretation of the Q4 signatures during MIS 11 versus MIS 7.

4. Discussion

4.1. Forcing of sGIS retreat

During glacial periods, the expanded sGIS is limited in extent by the continental shelf break (Bennike and Björck, 2002; Funder et al., 2011). Similar temporal baseline patterns in glacial maxima sand wt.% (Fig. 3i), Q3 silt signatures (Fig. 7), and Sr–Nd–Pb isotope composition (Figs. 6, 8) suggest the marine-terminating configuration of the sGIS may be largely consistent between glacial periods. From these expanded shelf-based glacial footprints, increases in radiative forcing and associated non-linear feedbacks (e.g., Past Interglacials Working Group of PAGES, 2016; Rohling et al., 2012) drove a warming climate through glacial terminations and ensuing interglaciations. Increases in summer boreal insolation were responsible for triggering the glacial terminations and were important for dictating the intensity of summer warming over Northern Hemisphere ice sheets (Carlson and Winsor, 2012; Huybers, 2011). While peak insolation provides a snapshot of maximum summer solar forcing within an orbital cycle (Tzedakis et

al., 2009), accumulated insolation incorporates the cumulative solar energy increase above the insolation minimum associated with a preceding glacial maximum (Carlson and Winsor, 2012), when we assume the sGIS was in equilibrium with glacial climate. By incorporating duration and intensity of orbital forcing, accumulated insolation may be a more meaningful measure of the progression and magnitude of deglaciation than simple peak boreal summer insolation (Carlson and Winsor, 2012). While boreal summer insolation has a seasonal effect on orbital-scale trends in summer warming over the sGIS, atmospheric CO_2 concentration modulates orbital-scale changes in mean-annual temperature (Lüthi et al., 2008; Tzedakis et al., 2009; Yin and Berger, 2010) and is an important component of total radiative forcing (Rohling et al., 2012) and indicator of interglacial warmth (Tzedakis et al., 2009). Comparison of CO_2 concentration and orbital forcing to our sGIS retreat proxies should therefore help establish the radiative threshold necessary to drive extensive sGIS retreat both off of the continental shelf and within its present-day margins.

4.2. sGIS response to forcing

Increases in radiative forcing through the glacial termination and interglaciation promotes increased ablation, leading to enhanced subglacial erosion and PG silt-laden runoff, and ultimately results in sGIS retreat (Carlson and Winsor, 2012; Cowton et al., 2012; Hanna et al., 2008; Tzedakis et al., 2009; Zwally et al., 2002). The lack of strong PG sourcing in both the magnetic and Sr–Nd–Pb isotopic datasets coupled with high levels of IRD indicates the sGIS likely occupied its largest interglacial footprint of the last five interglaciations during MIS 7, maintaining an extensive marine-terminating margin. The preceding T3 experienced the weakest accumulated insolation and CO_2 concentrations rarely exceeded ~250 ppm (Lüthi et al., 2008) (Fig. 8c), aside from a century-scale excursion to ~280 ppm during MIS 7e. As a result, the sGIS did not experience prolonged increased ablation and retreat. The greatest accumulated insolation of the last ~430 ka occurred during MIS 7d–7c, but there is no evidence for appreciable sGIS retreat (Fig. 8c). However, atmospheric CO_2 concentrations were near glacial levels during MIS 7d–7c, and likely limited the sGIS response to the accumulated boreal summer insolation forcing.

In contrast to MIS 7, low amplitude precession during MIS 11 initiated sustained increases in boreal summer insolation over 1.5 precession cycles, resulting in the second highest accumulated insolation (Fig. 8e) of the last five interglaciations. Atmospheric CO_2 concentration increased through the same interval and was at or above peak early Holocene values of ~265 ppm at ~426 ka (Lüthi et al., 2008) ~2 ka before T5 (Lisiecki and Raymo, 2005), which contributed to early and sustained interglacial radiative forcing over the sGIS lasting for ~30 ka (Rohling et al., 2012) (Fig. 8e). Peak MIS 11 Arctic summer temperatures may also have been 4–5 °C higher than during the Holocene (Melles et al., 2012). Accordingly, our magnetic and Sr–Nd–Pb isotope (Reyes et al., 2014) data imply near complete deglaciation of southern Greenland during MIS 11 before peak summer boreal insolation, suggesting that radiative forcing from atmospheric CO_2 strongly governs sGIS interglacial extent.

The forcing and subsequent sGIS response during the Holocene, MIS 5e, and MIS 9 are intermediate of the end-member cases of MIS 7 and MIS 11. Our sand wt.%, silt magnetic and Sr–Nd–Pb data show that although the sGIS retreated off of the continental shelf during all three terminations (T1, T2, T4), ice persisted on southern Greenland during the following Holocene, MIS 5e, and MIS 9 interglaciations (Figs. 8a, b, d). After a period of relatively low accumulated insolation, Holocene sGIS retreat slowed shortly after peak boreal summer insolation and atmospheric CO_2 concen-

trations of ~ 265 ppm (Lüthi et al., 2008). In contrast, eventual declines in summer boreal insolation did not halt sGIS retreat in the latter parts of MIS 5e and MIS 9, when atmospheric CO_2 remained above mean Holocene levels (Figs. 8b, d). Continued sGIS retreat under elevated atmospheric CO_2 during MIS 5e and 9 (relative to the early Holocene) implies that sGIS retreat was decoupled from boreal summer insolation and was sustained principally by atmospheric CO_2 forcing and associated feedbacks. Therefore, a stability threshold may have been crossed during MIS 5e and MIS 9 with sGIS retreat only slowing after reductions in atmospheric CO_2 and insolation as they approached MIS 5d and MIS 8, respectively (Figs. 8b, d). We consequently propose that the greater and longer combined orbital and atmospheric CO_2 forcing during MIS 11 allowed sGIS retreat to reach its equilibrium deglaciated state after crossing this ice-sheet stability threshold (Reyes et al., 2014; Robinson et al., 2012).

4.3. Implications for sGIS stability

Atmospheric CO_2 forcing appears to play a strong role in dictating the extent of the sGIS through the glacial terminations and interglaciations of the last ~ 430 ka. This assertion is supported by proxy data and climate model simulations of the last five interglaciations, which show that warmer interglacial climates during MIS 5e, 9 and 11 had higher atmospheric CO_2 relative to the Holocene and MIS 7e (Past Interglacials Working Group of PAGES, 2016; Tzedakis et al., 2009; Yin and Berger, 2010). Similarities in the progression of ice-sheet retreat, as reconstructed here from sediment, magnetic, and isotopic data, allow us to establish three modes of sGIS retreat. The first mode, experienced during MIS 7, exhibits little response to rising radiative forcing, with much of the sGIS maintaining a calving margin on the continental shelf. The second mode occurred during the Holocene, where retreat initially tracked rising radiative forcing, but then slowed during declining boreal summer insolation. Subsequent increases in CO_2 during the mid to late Holocene were not sufficient to reinvigorate sGIS retreat when facing declining insolation. A sufficiently strong combined CO_2 -insolation forcing through a glacial termination promotes the third mode of sGIS retreat that occurred during MIS 5e, MIS 9 and MIS 11, where a stability threshold is crossed that can lead to continued sGIS retreat despite subsequent decreases in insolation forcing. In the case of MIS 11, we suggest that the combined radiative forcing remained elevated long enough for the sGIS to retreat to its smallest extent of the last ~ 430 ka. We therefore propose that the threshold for sGIS deglaciation lies between the radiative forcing of the early Holocene and MIS 5e and MIS 9.

Due to proxy and age-model uncertainty, it is challenging to decipher the precise timing of forcing and ice-sheet response, particularly for T2 and earlier terminations (e.g. Marino et al., 2015). However, comparing the last five interglaciations and their radiative forcing allows us to conclude that atmospheric CO_2 concentrations above early Holocene peak values of ~ 265 ppm permit boreal summer insolation to drive the sGIS to a smaller-than-Holocene extent, as well as sustain sGIS retreat despite declining boreal summer insolation. In contrast, high boreal summer insolation during low- CO_2 interglaciations (as in MIS 7c–7a) (Fig. 8c) is insufficient to drive extensive sGIS retreat. In response to modest increases in radiative forcing relative to Holocene levels, the threshold for sGIS instability was likely crossed in three of the last five interglaciations over the last ~ 430 ka, one time causing near-complete deglaciation of southern Greenland during MIS 11. We consequently suggest that atmospheric CO_2 concentrations play a key role in modulating the extent of the sGIS. Our record of inferred sGIS response to radiative forcing over the last ~ 430 ka suggests that the Holocene extent and stability of the sGIS (Carlson et al., 2014; Larsen et al., 2015; Lecavlier et al., 2014) appears more

the anomaly than the rule in the context of the late Quaternary. Because of much higher modern atmospheric CO_2 levels relative to earlier interglaciations, the relatively large contemporary sGIS may be poised for substantial retreat despite the current minimum in boreal summer insolation.

Acknowledgements

This research was supported by US National Science Foundation awards ANS-0902571 (Carlson, Beard), ANS-0902751 and EAR-0651585 (Stoner) and the Natural Sciences and Engineering Research Council of Canada (Reyes; Discovery Grant 2015-03711). We thank Bernie Housen, Russ Burmeister, Chuang Xuan, and Jason Dorfman for help measuring the magnetic properties of the samples, and Weiqiang Li for assistance with Pb isotope analyses. We also thank the Captain, crew of the R/V Marion Dufresne II, and the scientific party of IMAGES V Leg II, for collecting core MD99-2227. Reviews by Ian Bailey and Nathalie Fagel improved this manuscript.

Appendix A. Supplementary material

Supplementary material related to this article can be found online at <http://dx.doi.org/10.1016/j.epsl.2016.09.014>.

References

- Barber, D.C., et al., 1999. Forcing of the cold event of 8200 years ago by catastrophic drainage of Laurentide lakes. *Nature* 400, 344–348.
- Bennike, O., Björck, S., 2002. Chronology of the last recession of the Greenland Ice Sheet. *J. Quat. Sci.* 17, 211–219.
- Carlson, A.E., 2008. Why was there not a Younger Dryas-like event during the penultimate deglaciation. *Quat. Sci. Rev.* 27, 882–887.
- Carlson, A.E., Winsor, K., 2012. Northern Hemisphere ice-sheet responses to past climate warming. *Nat. Geosci.* 5, 607–613.
- Carlson, A.E., Stoner, J.S., Donnelly, J.P., Hillaire-Marcel, C., 2008. Response of the southern Greenland Ice Sheet during the last two deglaciations. *Geology* 36, 359–362.
- Carlson, A.E., et al., 2014. Earliest Holocene south Greenland ice-sheet retreat within its late-Holocene extent. *Geophys. Res. Lett.* 41, 5514–5521.
- Channell, J.E.T., 1999. Geomagnetic paleointensity and directional secular variation at Ocean Drilling Program (ODP) Site 984 (Bjorn Drift) since 500 ka: comparisons with ODP Site 983 (Gardar Drift). *J. Geophys. Res.* 104, 22,937–22,951.
- Channell, J.E.T., Hodell, D.A., Xuan, C., Mazaud, A., Stoner, J.S., 2008. Age calibrated paleointensity for the last 1.5 Myr from IODP Site U1308 (North Atlantic). *Earth Planet. Sci. Lett.* 274, 59–71.
- Channell, J.E.T., Xuan, C., Hodell, D.A., 2009. Stacking paleointensity and oxygen isotope data for the last 1.5 Myr (PISO-1500). *Earth Planet. Sci. Lett.* 283, 14–23.
- Colville, E.J., et al., 2011. Sr–Nd–Pb isotope evidence for ice-sheet presence on southern Greenland during the last interglacial. *Science* 333, 620–623.
- Cowton, T., Nienow, P., Bartholomew, I., Sole, A., Mair, D., 2012. Rapid erosion beneath the Greenland ice sheet. *Geology* 40, 343–346.
- Cronin, T.M., et al., 2013. A 600-ka Arctic sea-ice record from Mendeleev Ridge based on ostracodes. *Quat. Sci. Rev.* 79, 157–167.
- Day, R., Fuller, M., Schmidt, V.A., 1977. Hysteresis properties of titanomagnetites: grain-size and compositional dependence. *Phys. Earth Planet. Inter.* 13, 260–267.
- de Vernal, A., Hillaire-Marcel, C., 2008. Natural variability of Greenland climate, vegetation, and ice volume during the past million years. *Science* 320, 1622–1625.
- Evans, H.F., et al., 2007. Paleointensity-assisted chronostratigraphy of detrital layers on the Eirik Drift (North Atlantic) since marine isotope stage 11. *Geochem. Geophys. Geosyst.* 8, Q11007. <http://dx.doi.org/10.1029/2007GC001720>.
- Fagel, N., Innocent, C., Gariépy, C., Hillaire-Marcel, C., 2002. Sources of Labrador Sea sediments since the last glacial maximum inferred from Nd–Pb isotopes. *Geochim. Cosmochim. Acta* 66, 2569–2581.
- Fagel, N., et al., 2004. Nd and Pb isotope signatures of the clay-size fraction of Labrador Sea sediments during the Holocene: implications for the inception of the modern deep circulation pattern. *Paleoceanography* 19, PA3002. <http://dx.doi.org/10.1029/2003PA000993>.
- Fagel, N., Hillaire-Marcel, C., 2006. Glacial/interglacial instabilities of the Western Boundary Undercurrent during the last 360 kyr from Sm/Nd signatures of sedimentary clay fractions at ODP-Site 646 (Labrador Sea). *Mar. Geol.* 232, 87–99.
- Funder, S., Kjeldsen, K.K., Kjaer, K.H., O Cofaigh, C., 2011. The Greenland ice sheet during the past 300,000 years: a review. In: Ehlers, J., Gibbard, P.L., Hughes, P.D. (Eds.), *Dev. Quat. Sci.*, vol. 15. Elsevier, Amsterdam, pp. 699–713.
- Galer, S.J.G., Abouchami, W., 1998. Practical application of lead triple spiking for correction of instrumental mass discrimination. *Mineral. Mag.* 62A, 491–492.

- Hall, F.R., Busch, W.H., King, J.W., 1989. The relationship between variations in rock-magnetic properties and grain size of sediments from ODP Hole 645C. In: Proc. Ocean Drill. Program Sci. Results, vol. 105. Ocean Drilling Program, College Station, Texas, pp. 837–841.
- Hanna, E., et al., 2008. Increased runoff for melt from the Greenland ice sheet: a response to global warming. *J. Climate* 21, 331–341.
- Hatfield, R.G., Stoner, J.S., Carlson, A.E., Reyes, A.V., Housen, B.A., 2013. Source as a controlling factor on the quality and interpretation of sediment magnetic records from the northern North Atlantic. *Earth Planet. Sci. Lett.* 368, 69–77.
- Helmke, J.P., Bauch, H.A., 2003. Comparison of glacial and interglacial conditions between the polar and subpolar North Atlantic region over the last five climatic cycles. *Paleoceanography* 18, 1036. <http://dx.doi.org/10.1029/2002PA000794>.
- Hillaire-Marcel, C., de Vernal, A., Bilodeau, G., Wu, G., 1994. Isotope stratigraphy, sedimentation rates, deep circulation, and carbonate events in the Labrador Sea during the last ~200 ka. *Can. J. Earth Sci.* 31, 63–89.
- Hodell, D.A., Channell, J.E.T., Curtis, J.H., Romero, O.E., Röhl, U., 2008. Onset of “Hudson Strait” Heinrich Events in the eastern North Atlantic at the end of the Middle Pleistocene Transition (~640 ka)? *Paleoceanography* 23, PA4218. <http://dx.doi.org/10.1029/2008PA001591>.
- Hunter, S., et al., 2007. Deep western boundary current dynamics and associated sedimentation on the Eirik Drift, Southern Greenland Margin. *Deep-Sea Res., Part 1* 54, 2036–2066.
- Huybers, P., 2011. Combined obliquity and precession pacing of the Pleistocene deglaciations. *Nature* 480, 229–232.
- Innocent, C., Fagel, N., Hillaire-Marcel, C., 2000. Isotope systematics in deep-sea sediments: clay-size versus coarser fractions. *Mar. Geol.* 168, 79–87.
- Larsen, N.K., et al., 2015. The response of the southern Greenland ice sheet to the Holocene thermal maximum. *Geology* 43, 291–294.
- Lecavlier, B.S., et al., 2014. A model of Greenland ice sheet deglaciation constrained by observations of relative sea level and ice extent. *Quat. Sci. Rev.* 102, 54–84.
- Lisiecki, L., Raymo, M.E., 2005. A Pliocene–Pleistocene stack of 57 globally distributed benthic $\delta^{18}\text{O}$ records. *Paleoceanography* 20, PA1003. <http://dx.doi.org/10.1029/2004PA001071>.
- Lüthi, D., et al., 2008. High-resolution carbon dioxide concentration record 650,000–800,000 years before present. *Nature* 453, 379–382.
- Marino, G., et al., 2015. Bipolar seesaw control on last interglacial sea level. *Nature* 522, 197–201.
- Mazaud, A., Channell, J.E.T., Stoner, J.S., 2012. Relative paleointensity and environmental magnetism since 1.2 Ma at IODP Site U1305 (Eirik Drift, NW Atlantic). *Earth Planet. Sci. Lett.* 357–358, 137–144.
- Melles, M., et al., 2012. 2.8 Million years of Arctic climate change from Lake El'gygytyn, NE Russia. *Science* 337, 315–320.
- Nicholl, J.A.L., et al., 2012. A Laurentide outburst flooding event during the last interglacial period. *Nat. Geosci.* 5, 901–904.
- Past Interglacials Working Group of PAGES, 2016. Interglacials of the last 800,000 years. *Rev. Geophys.* 54, 162–219.
- Reyes, A.V., et al., 2014. South Greenland ice-sheet collapse during Marine Isotope Stage 11. *Nature* 510, 525–528.
- Robinson, S.G., 1986. The late Pleistocene palaeoclimatic record of North Atlantic deep-sea sediments revealed by mineral-magnetic measurements. *Phys. Earth Planet. Inter.* 42, 22–47.
- Robinson, A., Calov, R., Ganopolski, A., 2012. Multistability and critical thresholds of the Greenland ice sheet. *Nat. Clim. Change* 2, 429–432.
- Rohling, E.J., et al., 2012. Sea surface and high-latitude temperature sensitivity to radiative forcing of climate over several glacial cycles. *J. Climate* 25, 1635–1656.
- Stanford, J.D., et al., 2006. Timing of meltwater pulse 1a and climate responses to meltwater injections. *Paleoceanography* 21, PA4103. <http://dx.doi.org/10.1029/2006PA001340>.
- Stoner, J.S., Channell, J.E.T., Hillaire-Marcel, C., 1995. Magnetic properties of deep-sea sediments off southwest Greenland: evidence for major differences between the last two deglaciations. *Geology* 23, 241–244.
- Stoner, J.S., Channell, J.E.T., Hodell, D.A., Charles, C.A., 2003. 580 kyr paleomagnetic record from the sub-Antarctic South Atlantic (ODP Site 1089). *J. Geophys. Res.* 108, 2244. <http://dx.doi.org/10.1029/2001JB001390>.
- Tzedakis, P.C., et al., 2009. Interglacial diversity. *Nat. Geosci.* 2, 751–755.
- White, L.F., et al., 2016. Tracking the provenance of Greenland-sourced, Holocene aged, individual sand-sized ice-rafted debris using the Pb-isotope compositions of feldspars and $^{40}\text{Ar}/^{39}\text{Ar}$ ages of hornblendes. *Earth Planet. Sci. Lett.* 433, 192–203.
- Winsor, K., Carlson, A.E., Klinkhammer, G.P., Stoner, J.S., Hatfield, R.G., 2012. Evolution of the northeast Labrador Sea during the last interglaciation. *Geochem. Geophys. Geosyst.* 13, Q11006. <http://dx.doi.org/10.1029/2012GC004263>.
- Yin, Q.Z., Berger, A., 2010. Insolation and CO_2 contributions to the interglacial climate before and after the Mid-Bruhnes Event. *Nat. Geosci.* 3, 243–246.
- Zwally, H.J., et al., 2002. Surface melt-induced acceleration of Greenland ice-sheet flow. *Science* 297, 218–222.